

Experimental and numerical investigations of mixed convection in turbine cavities for more flexible operations

Original article

Article history:

Submission date: 11 May 2022

Acceptance date: 7 June 2022

Publication date: 8 July 2022

This is the updated version of a paper originally presented at the Global Power and Propulsion Virtual Technical Conference, GPPS Xi'an21, April 11–13, 2022.



*Correspondence:

OM: oguzhan.murat@eng.ox.ac.uk

Peer review:

Single blind

Copyright:

© 2022 Murat et al. © This is an open access article distributed under the Creative Commons Attribution Non Commercial License (CC BY-NC 4.0), which permits unrestricted use, distribution, and reproduction in any medium for noncommercial purposes only, provided the original work is properly cited and its authors credited.

Keywords:

mixed convection; power generation; flexible operations; LES; facility design; heat transfer

Citation:

Murat O., Rosic B., Tanimoto K., and Egami R. (2022). Experimental and numerical investigations of mixed convection in turbine cavities for more flexible operations. *Journal of the Global Power and Propulsion Society*, 6: 106–123.
<https://doi.org/10.33737/jgpps/150751>

Oguzhan Murat^{1,*}, Budimir Rosic¹, Koichi Tanimoto², Ryo Egami²

¹Department of Engineering Science, Oxford Thermofluids Institute, University of Oxford, Oxford OX2 0ES, UK

²Mitsubishi Heavy Industries, Research and Innovation Centre, 2-1-1 Shinham Arai-Cho, Takasago 676-8686, Japan

Abstract

Since the renewable sources, which have gained great attention due to the low-carbon policies, are inherently intermittent, the conventional power generation systems will be in use to meet the power demand. These systems, however, must be capable of operating along with renewables, which will lead to a need for more operational flexibility with frequent system ramps. Therefore, understanding and control of thermal stresses and clearances are essential for improving flexibility of conventional power plants. Computational fluid dynamics tools are of great importance in predicting the turbomachinery flows design since the direct measurements of detailed and spatial flow and temperature distribution are often not trivial in the real engines. During shut-down regimes of steam turbines, natural convection takes place along with relatively weak forced convection which is not strong enough to prevent a rising thermal plume leading to a non-uniform cooling in the turbine cavities. Although natural and forced convection have been studied separately in the literature, mixed type of flows in turbine cavities have not been investigated extensively.

This paper provides unique experimental data set for validation and development of the predictive tools, which is generated from the detailed flow field measurements in a test facility designed for mixed type of flows in the turbine casing cavities with engine representative conditions. Additionally, large eddy simulations have been performed and validated against the generated experimental data, to gain deeper insight into the flow field. Thus, this paper offers a great insight in these complex flow interactions and unique experimental data for enabling the flexible operations and the development of advanced turbulence modelling.

Introduction

The fast uptake of renewable sources in power generation in the recent years has aggravated the problem of flexibility of conventional power generation systems. The intermittent nature of the renewable sources (solar and wind in particular) imposes new operational challenges for power plants which will be required to ramp more often with frequent shut-downs and start-ups. During the shut-down regimes, the turbine casing components are exposed to the buoyant flows with pure natural and mixed convection, which then lead to non-uniform cooling due to temperature non-uniformity on the components. Consequently, the non-uniform cooling rates may cause severe fatigue on the casing.

Considering these challenges, the first step towards addressing the issues would be ensuring that the flow physics during the shut-down regimes are thoroughly investigated. The experimental investigations, however, are often not feasible since the direct measurements in the flow field in the turbine cavities are not trivial. Therefore, majority of the observations heavily rely on computational methods. Although a large body of literature has sought to provide experimental data for pure natural (for example Beckmann (1931), Liu et al. (1961), Grigull and Hauf (1966), Kuehn and Goldstein (1976), and Fahy et al. (2018)) and forced convection (Brighton (1963), Farias et al. (2009) and Hosseini et al. (2009) among others), mixed type of convection in the turbine casing cavities has not been previously assessed to a broad extent. The experimental investigations concerning the mixed type type of flows have been mostly on fully developed duct and pipe flows (for example Kotake and Hattori (1985), Ciampi et al. (1987) and Mohammed et al. (2010)). In the recently conducted research of Murat et al. (2021), a unique experimental facility has been designed and commissioned for mixed type of flows in turbine casing cavities during shut-down regimes, and also incapacibilities of Reynolds-averaged Navier-Stokes (RANS) in predicting these type of flows have been highlighted by demonstrating the inadequacy of isotropic turbulence assumption.

The unavailability of the extensive experimental data, in return, ultimately reduces the confidence in the numerical results, which hinders the design optimization and the advance turbulence modelling development for the mixed type of flows.

Experimental methodology

Background

Mixed type of convection occurs in a wide range of turbomachinery applications, and are therefore of great importance. As mentioned earlier, especially high pressure (HP) steam turbine casing is exposed to both natural and mixed convection during shut-down regimes with different operating conditions. The cavity formed by the inner and outer turbine casings could be considered as a horizontal concentric annulus as seen in Figure 1 where various flow regimes taking place in the casing cavity are also presented.

In the case of pure natural convection, thermal plume occurs at the top of the heated inner cylinder, which rises and impinges on the outer casing. This leads to a non-uniform cooling. After impingement, the fluid cools down and moves down the lower portion of the annulus where the flow tends to be stable. When the pure forced convection takes places, a circumferentially uniform boundary layer forms around the inner cylinder as shown in Figure 1. The flow behaviour in the upper portion of the annulus significantly changes when both natural and forced convection take place simultaneously. The thermal plume region is distorted by the cross-flow, and multiple longitudinal structures develop due to the complex flow interactions.

Experimental facility

An experimental facility illustrated in Figure 2 has been designed for the detailed investigations of mixed (natural and forced) convective type of flows in a simplified turbine casing cavity represented by a horizontal concentric annulus. The inner casing temperature is kept constant by a PID controller at a set value, while the incoming air speed is varied by an industrial blower at the outlet for different mixed convection rates. Low conductivity calcium silicate inserts are used at both end of the inner cylinder, which is made of copper, to minimise the heat loss. Self-adhesive ceramic heat shields have been placed around the outer casing cylinder to reduce the heat dissipation. The facility consists of various measurement ports distributed axially and circumferentially. Measurement locations on the test facility are depicted in the facility schematic in Figure 3 and some of the essential dimensions are tabulated in Table 1. The detailed design information regarding the experimental facility can be found in the study of Murat et al. (2021).

For pure natural and forced convective flows, Grashof and Reynolds numbers are important non-dimensional parameters to determine the flow regime. Richardson number is used when both natural and forced convection take place simultaneously. The non-dimensional numbers used in the present study are given in Equation 1.

$$Gr_{L_g} = \frac{g\beta(T - T_\infty)L_g^3}{\nu^2}, Re_{D_b} = \frac{uD_b}{\nu}, Ri = \frac{Gr}{Re^2} \quad (1)$$

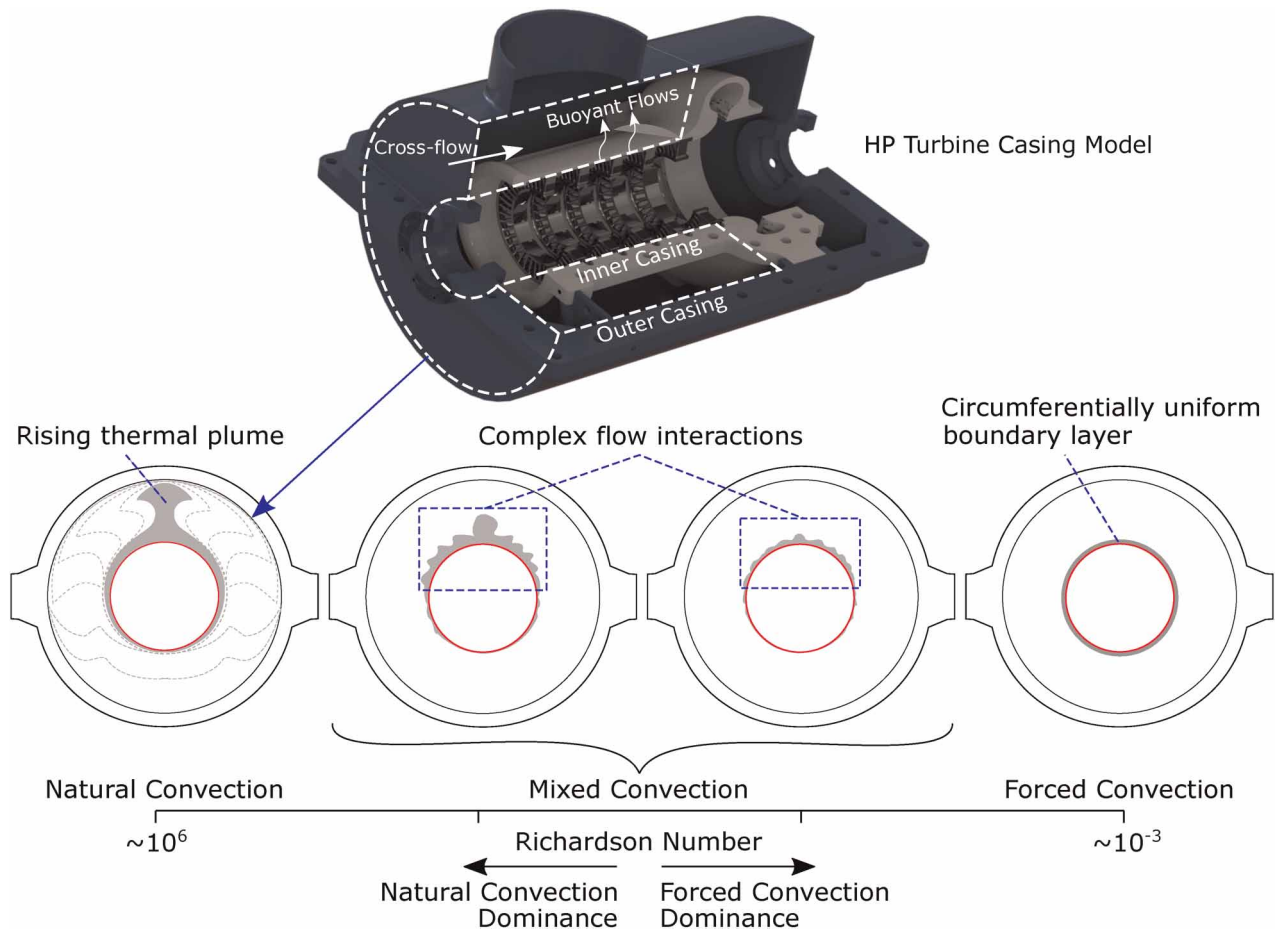


Figure 1. Variation of flow regimes in casing cavities.

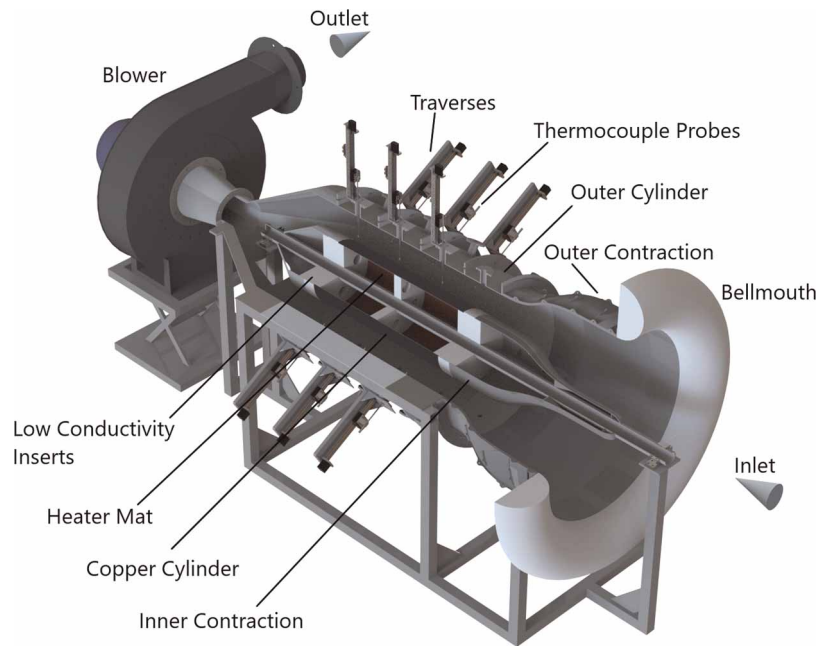


Figure 2. Cross-section of the test facility CAD model.

It is important that a test facility is able to operate at real engine representative conditions to have realistic conditions. In the present study, the test facility is capable of operating at various mixed convective flow regimes as well as pure natural and forced convective flows. Figure 4 shows the range that the facility can operate in

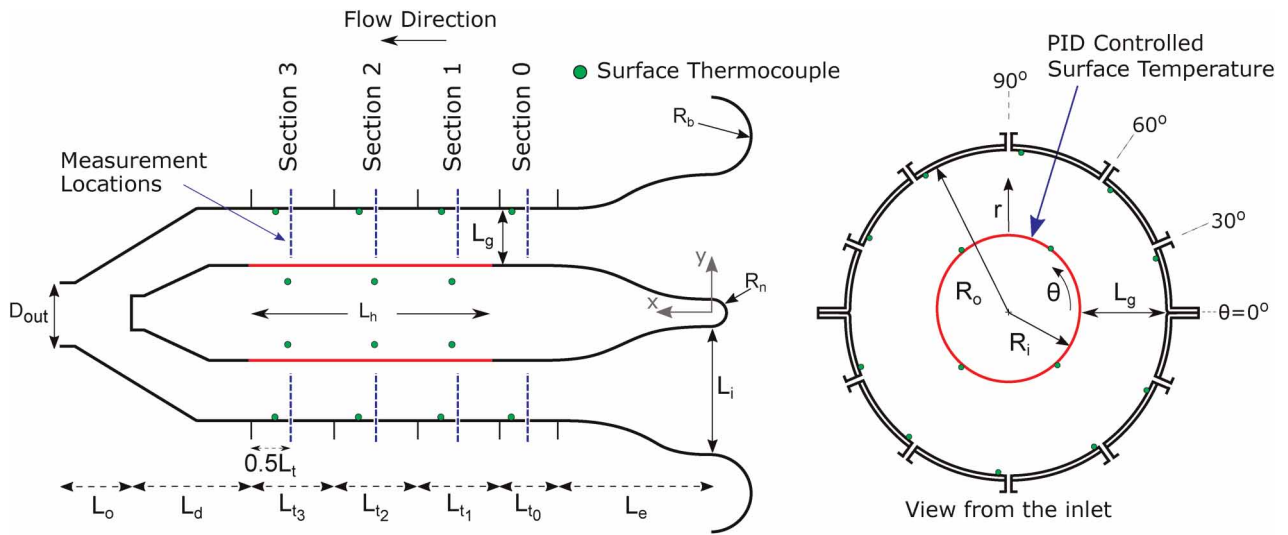


Figure 3. Experimental facility schematic and measurement locations.

Table 1. Rig dimensions.

Parameter	Dimension (mm)	Parameter	Dimension (mm)	Parameter	Dimension (mm)	Parameter	Dimension (mm)
R_i	180	R_n	70	L_e	720	L_d	425
R_o	400	L_i	440	L_{t_0}	250	L_o	390
R_b	150	L_g	220	$L_{t_{1,2,3}}$	300	D_{out}	200

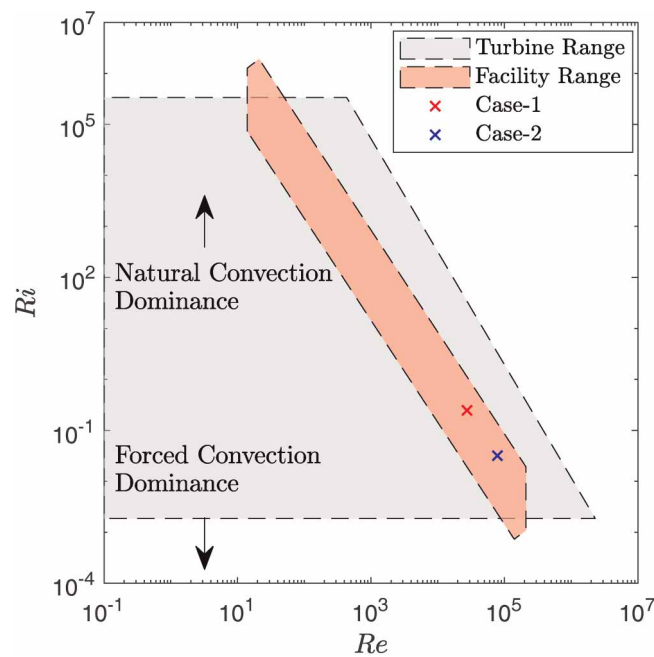


Figure 4. Experimental facility operation range.

comparison with the real turbine data during a shut-down regime, which indicates that the facility is capable of reproducing engine realistic conditions. In the same figure, mixed type of flow cases that are presented in this paper are also marked, the details of which are tabulated in Table 2.

Linear actuators with accuracy of 0.05 mm have been used to traverse the thermocouple probes, which are distributed in axial and circumferential locations. The thermocouple probe houses two K-type thermocouples and a needle to keep the thermocouple beads at a known distance from the heated copper cylinder, as shown in Figure 5. During the measurements, the thermocouple probes were traversed starting from the heated inner cylinder towards the outer cylinder. Step of 0.1 mm was used near the heated wall to be able to capture the near-wall gradients, while relatively larger steps were used away from the walls. Time averaging of unsteady data acquired by National Instruments data acquisition modules was performed over 120 seconds with 50 Hz sampling rate.

Although the heated copper cylinder is covered with a mat black paint, the radiation effect may still be significant. When the heat conduction through the thermocouple sheath tube is ignored, the energy balance applied on a thermocouple bead consists of convective and radiative heat transfer as shown in Equation 2. Measurement or estimation of the effective surrounding temperature, T_{eff} is required to calculate the true fluid temperature, T_f , however it is usually not possible. Therefore, it should somehow be eliminated from the equation. To do so, another thermocouple with different diameter but the same thermophysical properties can be used by relating two energy balance equation for each thermocouple bead (Tagawa and Ohta, 1997; Brohez et al., 2004; Kim et al., 2010).

$$h(T_f - T_b) = \varepsilon_b \sigma (T_b^4 - T_{eff}^4) \quad (2)$$

Table 2. Experiment characteristics.

Parameter	Case-1	Case-2
Gr_{L_g}	1.86×10^8	1.96×10^8
Re_{D_h}	2.75×10^4	7.87×10^4
$Ri(Gr_{L_g}/Re_{D_h}^2)$	0.246	0.032

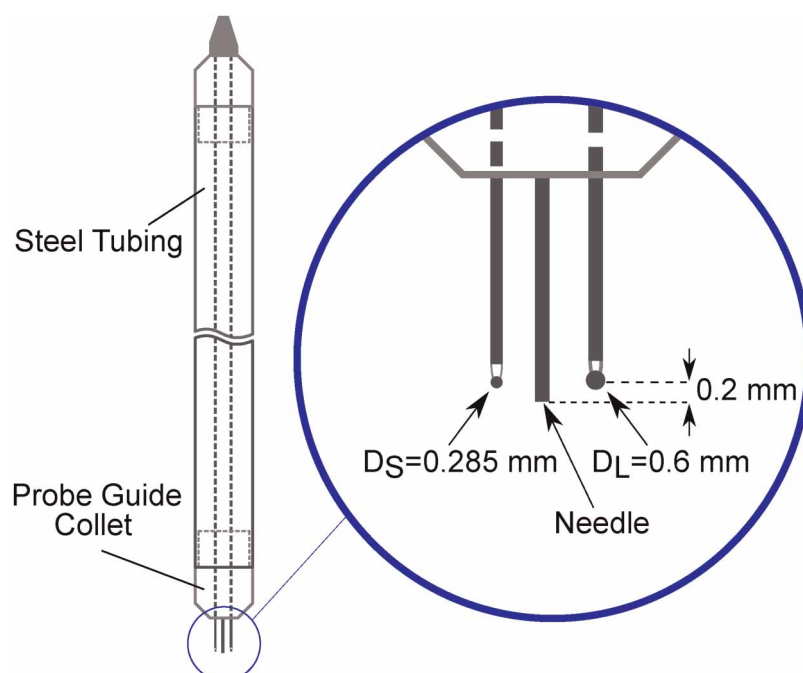


Figure 5. Thermocouple probe.

Numerical methodology

Large Eddy Simulations (LES) have been performed for mixed convection experiments to further investigate the flow field with ANSYS Fluent (ANSYS, 2020). Pressure-velocity coupling is maintained with the SIMPLE algorithm with a segregated manner. Second order scheme has been used for pressure discretisation. A bounded central differencing scheme has been used for momentum and energy. A bounded second order implicit scheme has been chosen for the temporal discretisation. Dynamic Smagorinsky model (Germano et al., 1990) has been employed for sub-grid scale modelling. Large eddy simulations were initialized using the flow field predicted by RANS simulations.

Two conformal structured hexahedral type meshes with 29.6 and 25.3 million nodes have been used for Case-1 and Case-2, respectively. Detailed information on mesh resolutions in wall units is given in Tables 3 and 4.

Time steps of $\Delta t_1 = 2 \times 10^{-3}$ s and $\Delta t_2 = 5 \times 10^{-4}$ s have been used for Case-1 and Case-2, respectively. Both simulations yielded $CFL < 0.5$. For each case, the simulation had been run until it reached statistically steady state before sampling the unsteady data. Convergence was ensured by monitoring unsteady data at several points in the test section. Initial transients decayed after about 5 flow-through times at each case, then the statistics were collected for 14,000 and 8,000 time steps for Case-1 and Case-2, respectively. The properties of the fluid (air), which was treated as incompressible ideal gas, used for each simulation case are tabulated in Table 5. The fluid properties were evaluated at the ambient condition for each case which read as $P_{\infty 1} = 1.003$ bar and $P_{\infty 1} = 295.65$ K for Case-1, and $P_{\infty 2} = 1.002$ bar and $P_{\infty 2} = 294.65$ K for Case-2.

Figure 6 shows the amount of resolved turbulent kinetic energy at Section 3 - $\theta = 90^\circ$ at each case, which indicates that the grid resolution in both cases is sufficient to resolve the significant amount (average of 95%) of the turbulent kinetic energy. Energy spectra of the stream-wise velocity fluctuations are presented in Figure 7

Table 3. Case-1 mesh resolution.

	Δx^+	$R_i \Delta \theta^+$	$R_o \Delta \theta^+$	$0 < r^+ < 284.1$		$284.1 < r^+ < 568.2$		$568.2 < r^+ < 852.36$	
				Δr_{\min}^+	Δr_{\max}^+	Δr_{\min}^+	Δr_{\max}^+	Δr_{\min}^+	Δr_{\max}^+
Case-1	17.07	18.22	40.51	0.29	3.45	3.45	7.58	1.16	9.52

Table 4. Case-2 mesh resolution.

	Δx^+	$R_i \Delta \theta^+$	$R_o \Delta \theta^+$	$0 < r^+ < 147.2$		$147.2 < r^+ < 1027.6$		$1027.6 < r^+ < 1366.8$	
				Δr_{\min}^+	Δr_{\max}^+	Δr_{\min}^+	Δr_{\max}^+	Δr_{\min}^+	Δr_{\max}^+
Case-2	23.53	25.02	55.61	0.31	4.18	4.18	30.4	1.24	24.3

Table 5. Fluid properties.

Case	k (W/mK)	C_p (J/kgK)	μ (kg/ms)	Pr	β (1/K)
Case-1	0.02587	1006.906	1.84×10^{-5}	0.7144	3.39×10^{-3}
Case-2	0.02579	1006.864	1.83×10^{-5}	0.7146	3.41×10^{-3}

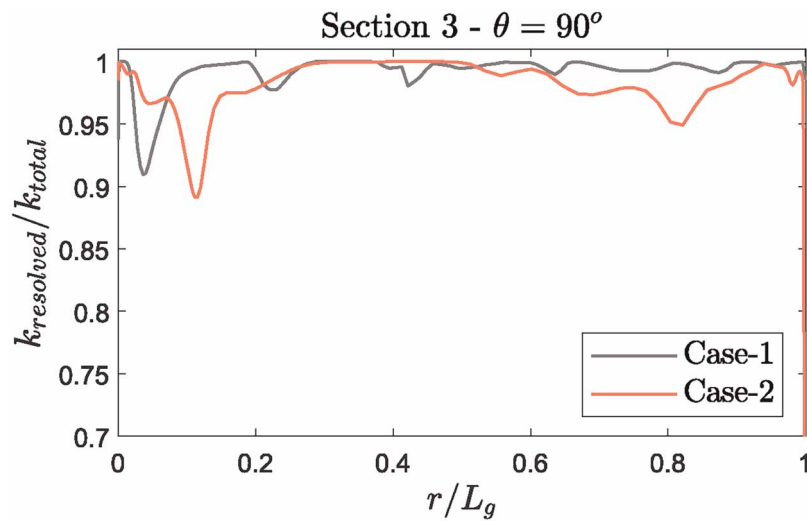


Figure 6. Resolved turbulent kinetic energy.

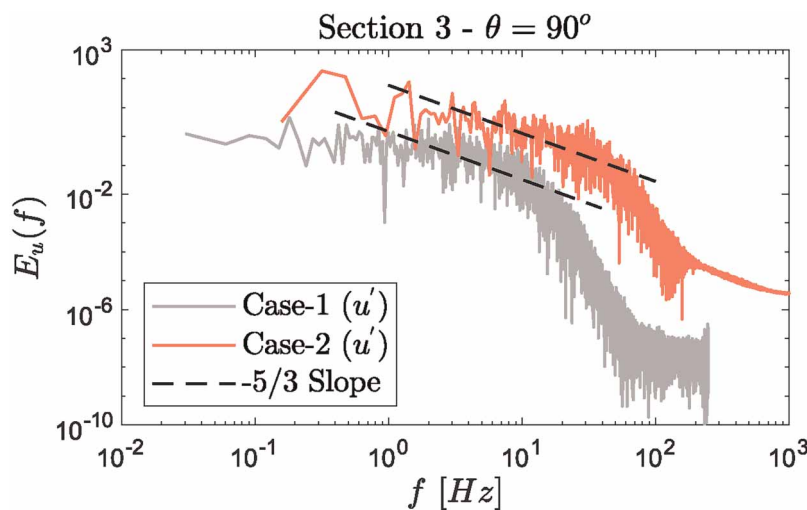


Figure 7. Energy cascade at $r/L_g = 0.9\%$.

where both cascades agree with the Kolmogorov's $-5/3$ slope in the inertial sub-range which further verifies the simulations.

Boundary conditions

The computational domain used for LES is illustrated in Figure 8. As seen in the figure, CFD domain involve a region at upstream of the bellmouth, referred as “entrance region”, to allow boundary layer development over the bellmouth. Mass flow rate for each case has been calculated using the air speed measured at Section 0 by hot-wire anemometry, which read as $\dot{m}_1 = 0.46$ kg/s and $\dot{m}_2 = 1.31$ kg/s for Case-1 and Case-2, respectively. For the inlet boundary conditions, the ambient conditions have been used. Isothermal wall condition has been applied to inner and outer cylinder walls in the test section, and the details of the boundary conditions are given in Table 6. The remaining walls in the domain have been treated as adiabatic walls.

Heat transfer measurement and uncertainty analysis

This section explains how the heat fluxes from the heated inner cylinder and the Nusselt numbers are calculated from the raw measurement data in this study. In the viscous sub-layer, the heat transfer occurs only through

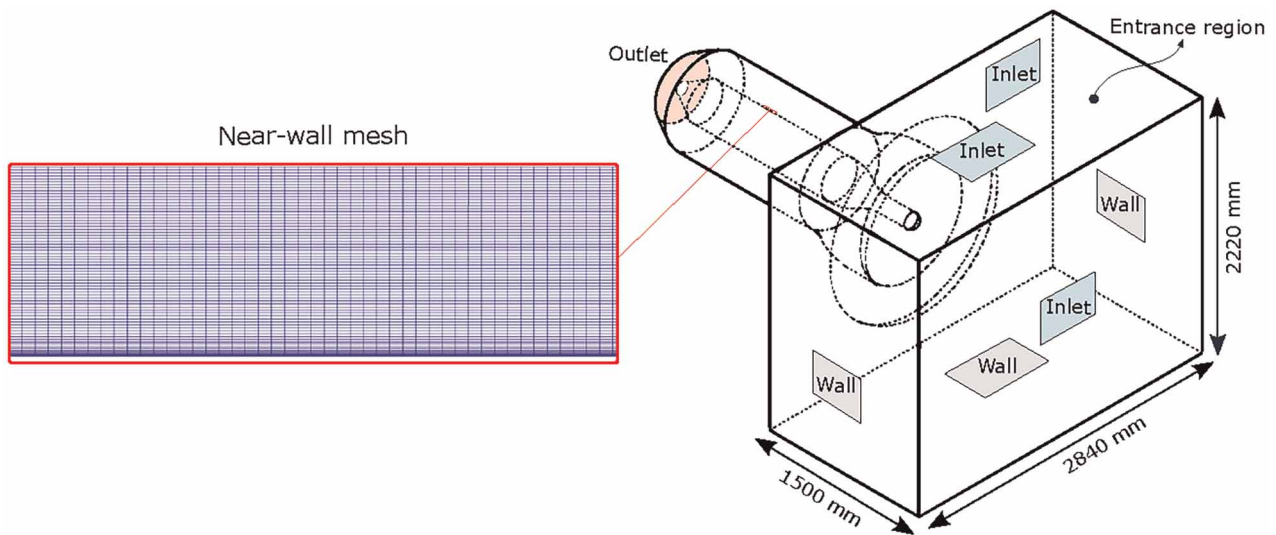


Figure 8. Computational domain.

Table 6. Test section wall boundary conditions.

Test Section		Case-1 (K)	Case-2 (K)
Heated inner cylinder		422.5	426.5
Section 1 Outer Casing	Lower Half	315.5	308.1
	Upper Half	314.5	307.1
Section 2 Outer Casing	Lower Half	320.6	313.1
	Upper Half	318.6	313.1
Section 3 Outer Casing	Lower Half	316.1	311.1
	Upper Half	317.6	311.1

conduction when the radiation is neglected. Temperature field exhibits the same characteristics as the velocity field (Schlichting and Gersten, 2017). Therefore, the temperature gradient remains linear in the viscous sub-layer, and the heat flux from a solid surface to a fluid can be calculated by Fourier's law ($q'' = -k \, dT/dr$). The heat transfer results are presented in Nusselt number form as shown in Equation 3.

$$Nu = \frac{q'' D_i}{(T_i - T_\infty)k} \quad (3)$$

In the experiments, the temperature gradients were captured using small traverse stepping (0.1 mm) near the heated wall. The near-wall measurement points in the radial direction at each traverse location were fitted to a straight line, and the slope of the each line was used to calculate the heat flux. Fittings were performed using linear regression analysis.

Figure 9 shows the near wall temperature gradient at $\theta = 90^\circ$ at Section 3 (the other locations are not shown for brevity). The measurement and LES of Case-1 points used in the linear fittings are highlighted. Straight lines created using the best fit are also illustrated, which are used for evaluating the goodness of the fit, R^2 .

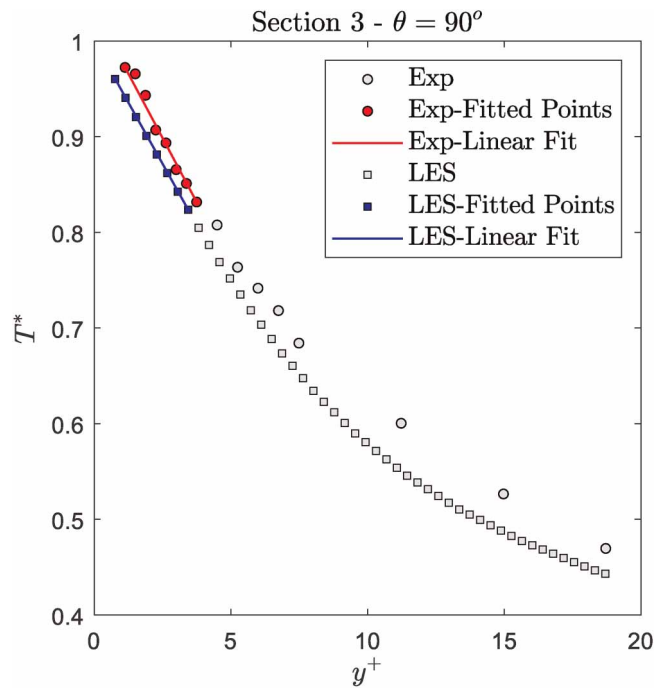


Figure 9. Near-wall temperature gradient fit.

In Figure 10, how the experimentally and numerically calculated Nusselt number varies depending on the end point selection is shown. In order to judge the goodness of the fits, R^2 values corresponding to both the experiment and LES are also presented in Figure 10 with respect to the right-hand y-axis. The selected LES data points follow a straight line up to $y^+ \approx 5$ as seen in Figure 9. Figure 10 confirms the goodness of the LES data point fit. Looking at the experimental data points, the R^2 values vary remarkably depending on the end point selection since the measurement points do not align as straight as LES data due to the experimental uncertainties.

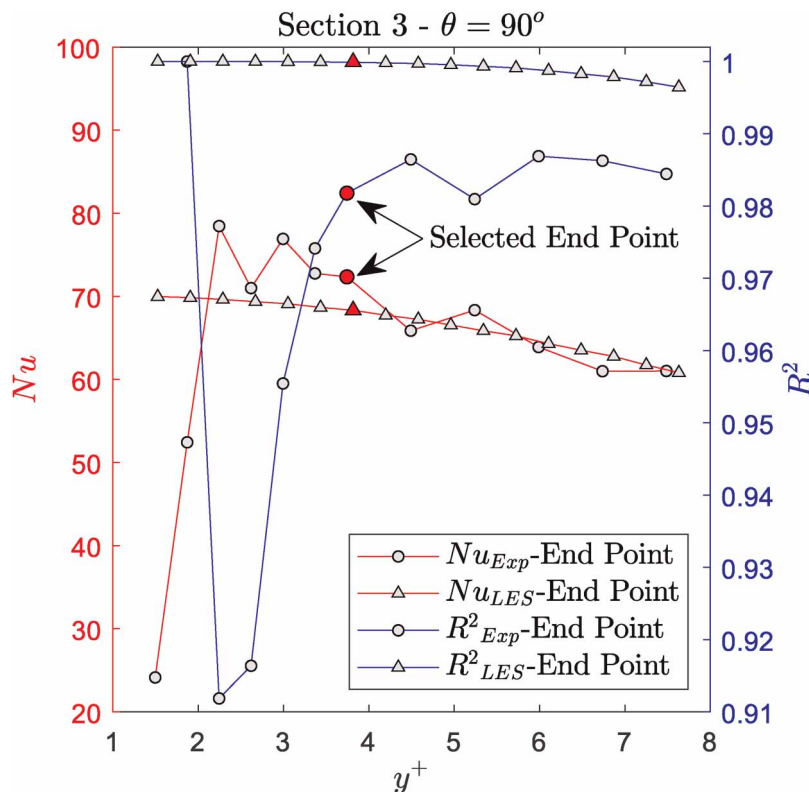


Figure 10. Nusselt number and R^2 variation.

The selected experimental end point is at $y^+ \approx 4$ which is close to the viscous sub-layer limit at $y^+ = 5$. LES R^2 values also confirms the adequacy of the location of the selected point as R^2 starts deviating from $R^2 = 1$ after $y^+ \approx 4$.

The experimental heat flux calculation requires detailed analysis at each measurement point since the viscous sub-layer thickness varies around the heated inner cylinder. In addition, the number of points used for line fitting may change remarkably, which consequently leads to the different uncertainties in Nusselt number around the inner cylinder as shown in Figure 11. The associated bias errors for each variable used in Nusselt number calculation are given in Table 7. The uncertainty analysis has been conducted using root sum square method (Moffat, 1988) as shown in Equation 4. The number of points used for the heat flux calculation effects the uncertainty in Nusselt number calculation remarkably since the the heat flux term, q'' includes the temperature gradient term where Δr is crucial. The uncertainty due to the Δr term increases greatly when only few points are used for the linear fit since the size of Δr converges to the accuracy of the traverse system. Therefore, a great attention must be paid when calculating the experimental heat flux. To illustrate how significantly Nusselt

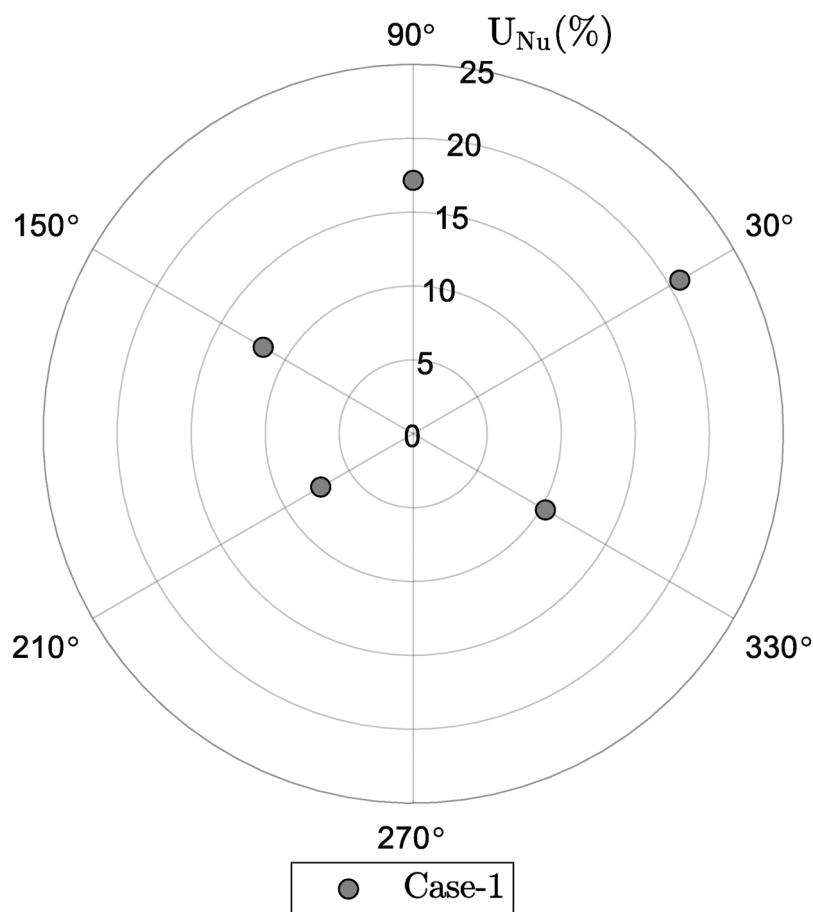


Figure 11. Uncertainty variation at Section 3.

Table 7. Bias error of each variable.

Variable	Uncertainty	Variable	Uncertainty
Traverse Thermocouple	± 0.5 K	Heated Cylinder Diameter	± 1 mm
PID Thermocouple	± 0.5 K	Traverse	± 0.05 mm

number uncertainty may vary, the variation in the present study is shown in Figure 11.

$$B_{Nu} = \sum_n \sqrt{\left(\frac{\partial Nu_{D_i}}{\partial V_n}\right)^2 B_{V_n}^2} \quad (4)$$

Figure 12 indicates the distance from $y^+ = 5$ around the inner cylinder in both Case-1 and Case-2. Since the large thermal plume does not form in Case-2 due to the strong cross-flow, the viscous sub-layer is much thicker in Case-1 than Case-2. The relatively thin viscous sub-layer in Case-2 has reduced the accuracy of the heat flux calculations due to the insufficient number of data points to be fitted. As previously mentioned, the thermocouple is placed 0.2 mm away from the wall. Considering the size of the thermocouple bead ($D_S = 0.285$ mm), the first measurement has been ignored to avoid wall proximity effects on the temperature readings, therefore the first measurement point is located 0.3 mm away from the wall. For instance, looking at $y^+ = 5$ location in Case-2 which reads ~ 0.7 mm, the remaining 0.4 mm was not enough to perform multiple thermocouple traversing, and therefore the accurate heat flux calculations could not be performed for Case-2.

Results and discussion

Temperature profiles

Temperature profiles are presented in a non-dimensional form as $T^* = ((\bar{T} - T_\infty)/(T_i - T_\infty))$. Figure 13 illustrates the qualitative comparison of the flow fields predicted by LES for buoyancy dominant Case-1 and forced convection dominant Case-2. The most prominent difference between the two cases is the growing thermal plume development at the top. In Case-1, the buoyancy forces are strong enough to cause upward flow movement at the top of the inner cylinder. In Case-2, on the other hand, the thermal plume is not formed due to the strong cross flow, therefore leading to more uniform thermal boundary layer thickness around the inner cylinder than Case-1. The lower portion of the annulus in both cases resembles each other with thin laminar boundary layer as also reported in the study of Murat et al. (2021).

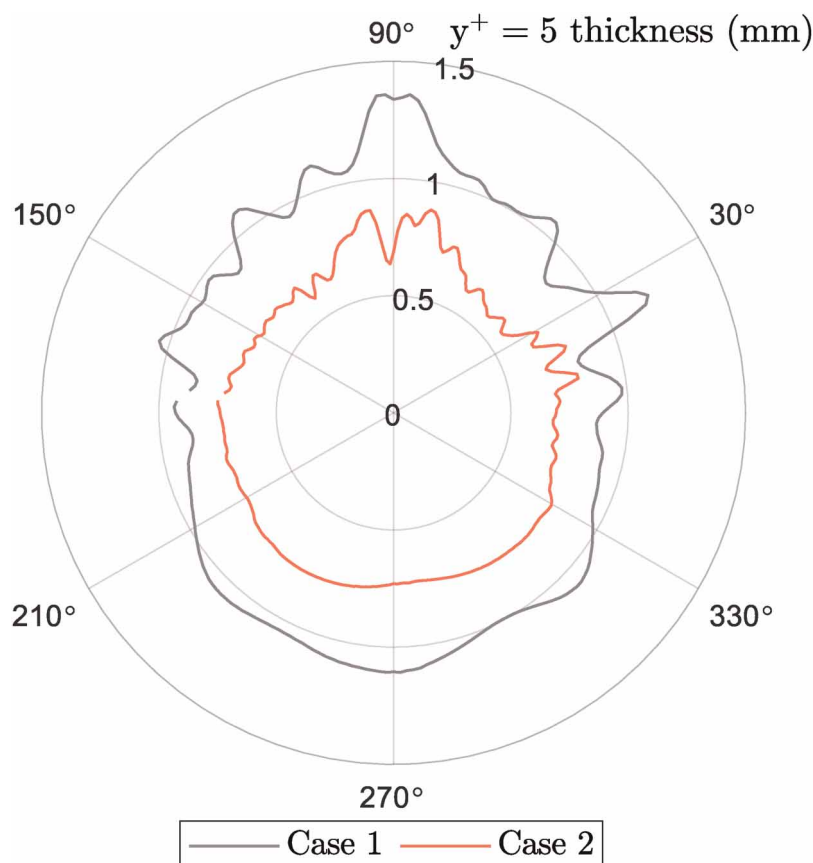


Figure 12. Sublayer thicknesses at Section 3.

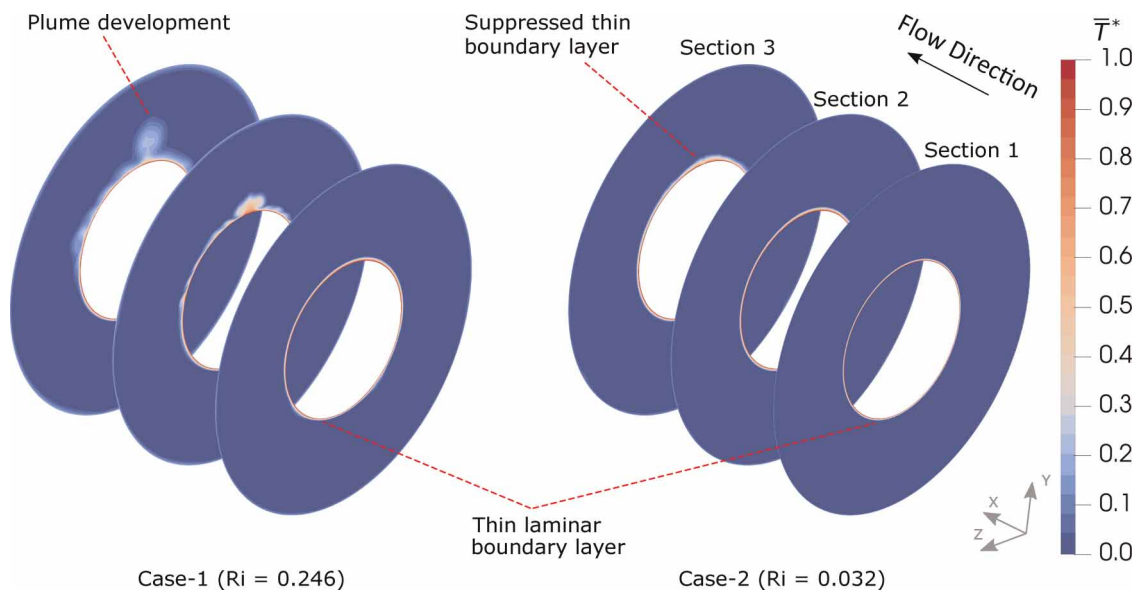


Figure 13. Time-averaged temperature contours.

Time-averaged non-dimensional temperature profiles predicted by LES are compared against the experimental data in Figure 14 for Case-1 at Section 1, 2 and 3. At Section 1, the thin temperature boundary layer is present around the inner cylinder, indicating that the buoyancy effect is not strongly pronounced at this section. Good agreement between numerical and experimental results has been achieved at Section 1. As the fluid progresses, the development of the boundary layer becomes noticeably distinguishable at the top of the annulus at $\theta = 90^\circ$ at Section 2. The thickening of the boundary is also present at both sides at $\theta = 30^\circ$ and 150° . The lower portion of the annulus still exhibits a thin boundary layer. Although LES has over-predicted temperature profile at $\theta = 90^\circ$, there has been satisfactory agreement between LES and the experiment. Towards the downstream of the test section, the thermal plume is further developed at Section 3, resulting in the thickest boundary layer at $\theta = 90^\circ$. The buoyancy effect is also present at $\theta = 30^\circ$ and 150° with thicker boundary layers compared to those at Section 1 and 2. The lower portion of Section 3 resembles Section 1 and 2 with a thin boundary layer caused by the buoyancy forces forcing the flow move up against the bottom of the inner cylinder. Overall, LES results agree well with the experimental results at Section 3.

Figure 15 shows the temperature profiles from LES and the experiment for Case-2. As opposed to Case-1, Case-2 represents strong momentum of the fluid in the axial direction which reduces the effect of the buoyancy. At Section 1, there is a uniform temperature boundary layer around the inner cylinder which is well predicted by LES. At Section 2, the boundary layer is slightly thickened around the inner cylinder, however the temperature profiles at all measurement locations are very similar, which elucidates the dominance of the forced convection. This flow behaviour can also be seen in Figure 13 where there is no sign of clear plume development. At the upper portion of the annulus at Section 3, the temperature boundary layer is slightly thicker than the lower portion. However, the thermal plume is still not present, therefore the temperature profiles in the annulus are not radically different. Overall, LES has exhibited a good agreement with the experimental data at all sections in Case-2.

Flow field

The flow field in the annulus can be investigated with the iso-surfaces and their footprints on the heated inner cylinder as illustrated in Figure 16 where the iso-surfaces of the second invariant of velocity ($Q = 0.5(W^2 - S^2)$) and the time-averaged wall shear stress on the inner cylinder are shown for each case. In the upstream of the inner cylinder, Case-1 exhibits laminar flow region where the buoyancy is not strongly pronounced in the upper half. As the flow progresses, hairpin-like vortices are formed which causes early transition to turbulence and the thermal plume lift-off at $\theta = 90^\circ$. This can also be observed in the reduced wall shear stress at the top of the inner cylinder in 16b. On the sides of the inner cylinder between $\theta = 0^\circ - 70^\circ$ and $\theta = 110^\circ - 180^\circ$, some of the low momentum fluid near the heated inner cylinder lifts-off due to buoyancy and is stretched towards the downstream by the cross-flow. After the detachment, the fluid shows tendency to

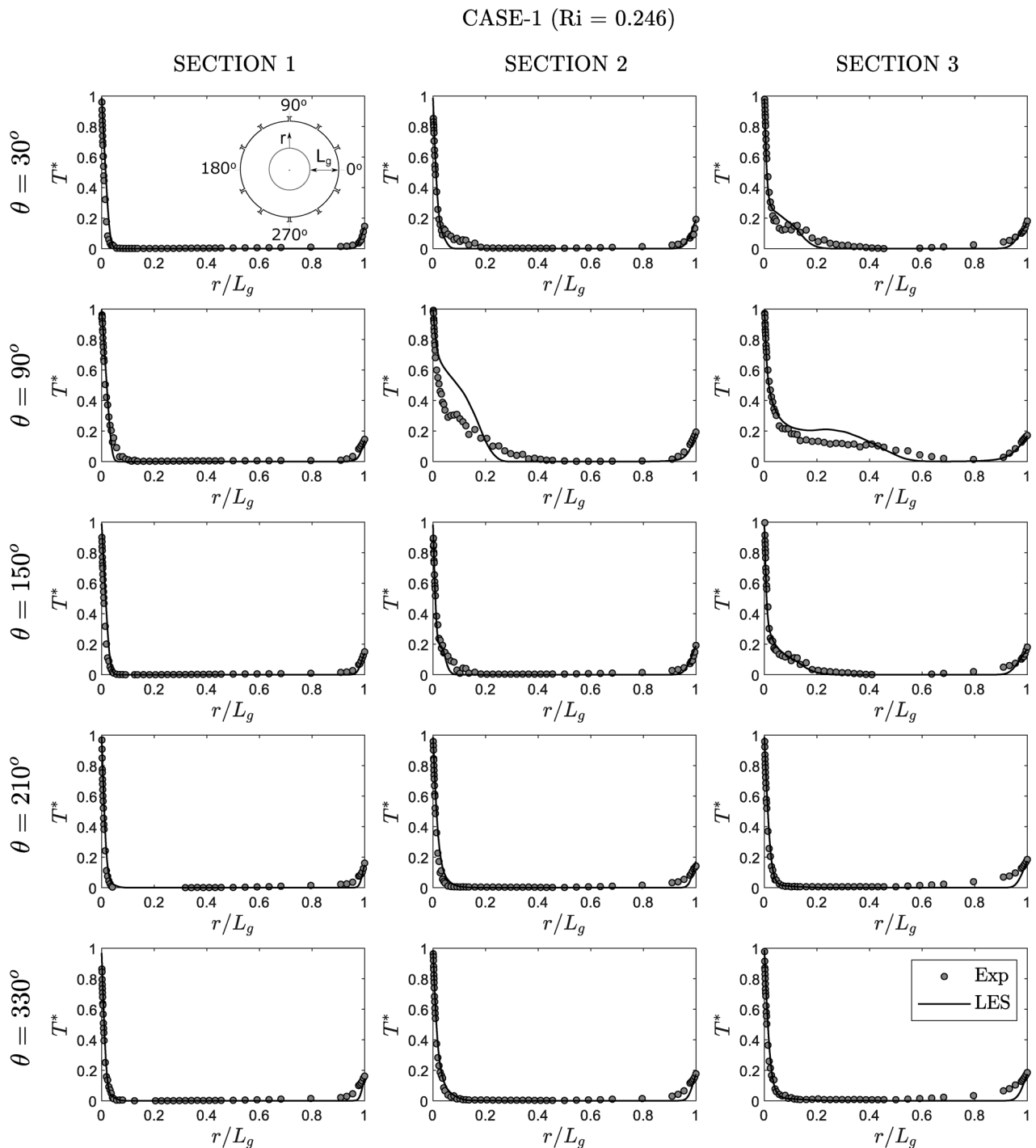


Figure 14. Time-averaged temperature profiles of Case-1 (Ri = 0.246).

move downwards due to a decrease in the temperature, and then re-join the near-wall low-momentum fluid that moves upwards. Therefore, longitudinal helical structures, which enlarge along the stream-wise direction, form as shown in Figure 16a. These flow structures can be tracked by looking at their footprints on the inner cylinder as illustrated in Figure 16b where the stretched streaks are seen.

As opposed to Case-1 which represents a strong buoyancy influence in the flow field, Case-2 exhibits strong cross-flow influence which minimises the buoyancy effect. This phenomenon can be observed by looking at Case-2 iso-surfaces in 16a where the thermal plume is not formed at $\theta = 90^\circ$ due to the strong inertial force. Boundary layer instabilities are present in the upstream of the inner cylinder due to the relatively high speed flow. Towards the downstream, the low momentum buoyant flows near the inner cylinder are convected to the top of the inner cylinder. However, these near-wall fluid movements remain as instabilities as seen in Figure 16

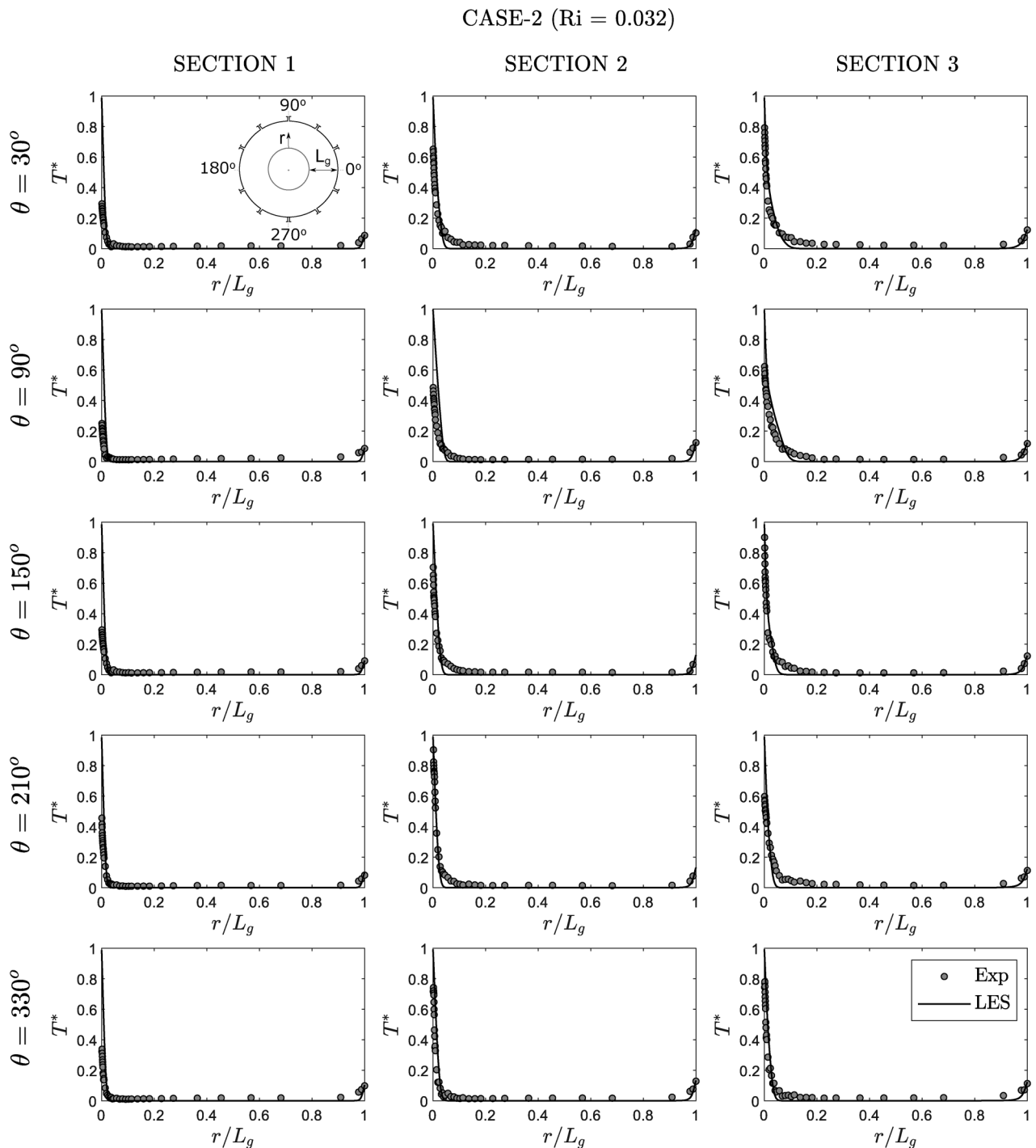


Figure 15. Time-averaged temperature profiles of Case-2 (Ri = 0.032).

where there is no sign of developed vortices. In the downstream, the turbulent region exists as seen in locally increased/decreased wall shear stress.

Although the lower portion of the annulus remains laminar with both cases, there is a locally increased wall shear stress at the bottom of the inner cylinder in Case-1 due to the buoyant forces pushing the flow upwards against the inner cylinder which suppress the growth of the boundary layer. The shear stress distribution in Case-2 remains relatively uniform until the beginning of the turbulent region.

Heat transfer

Table 8 shows the detailed information on Nusselt number distribution at circumferential and axial measurement locations, which could be used for validation purposes. For Case-1, experimentally and numerically calculated Nusselt numbers as well as the LES errors are tabulated. Since the experimental heat transfer could not be

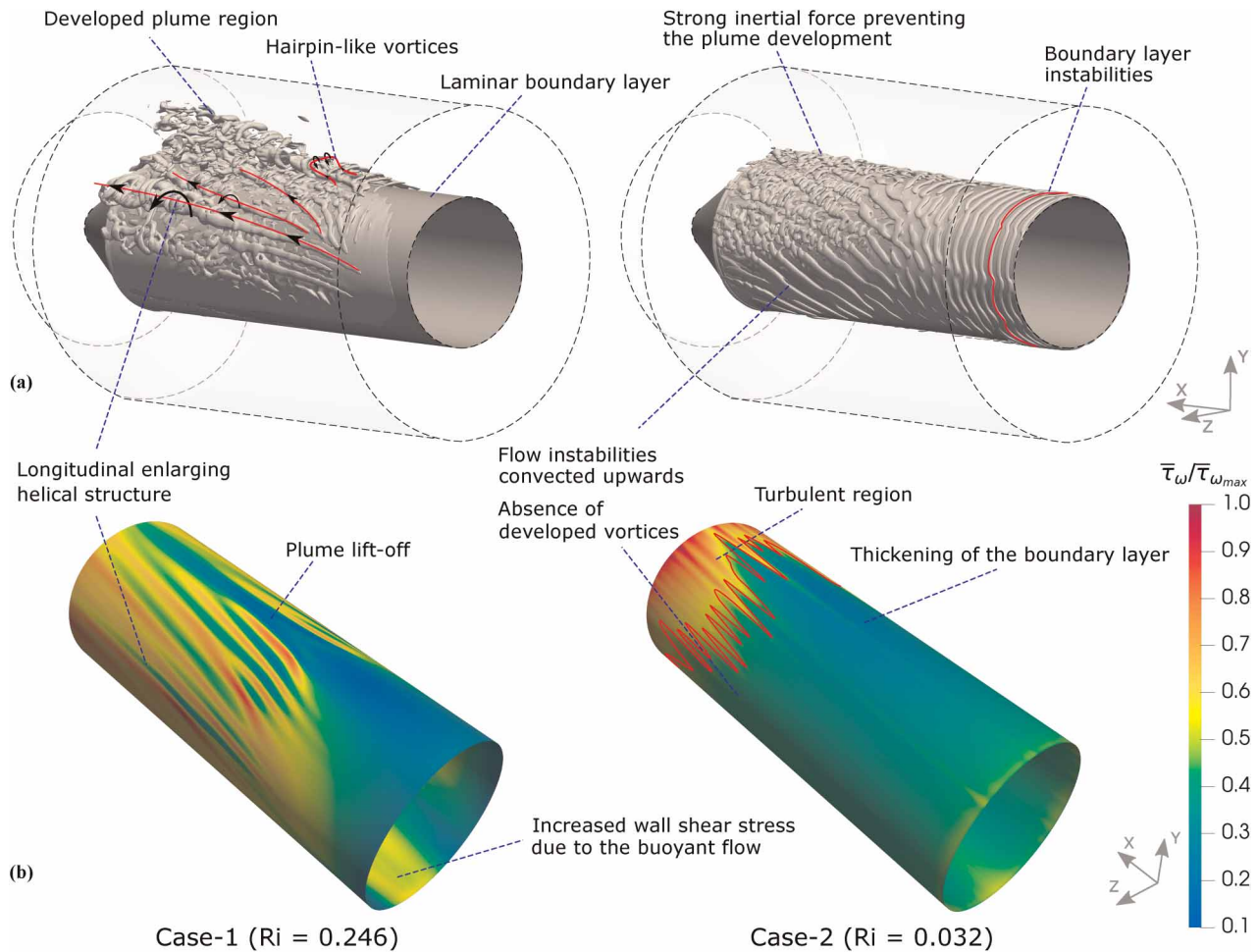


Figure 16. (a) Iso-surfaces of second invariant of velocity, (b) Time-averaged wall shear stress around the inner cylinder.

Table 8. Inner cylinder Nusselt number comparison.

θ	Section 1				Section 2				Section 3			
	Exp-1	LES-1	E-1 (%)	LES-2	Exp-1	LES-1	E-1 (%)	LES-2	Exp-1	LES-1	E-1 (%)	LES-2
30°	53.29	54.01	1.33	98.51	69.97	66.81	-4.74	65.27	86.51	93.88	7.85	97.35
90°	40.53	41.54	2.43	90.25	42.01	34.95	-20.19	46.47	72.34	70.19	-3.07	89.73
150°	52.85	53.75	1.67	97.27	90.99	96.80	6.01	62.93	104.11	106.01	1.78	99.38
210°	73.88	84.06	12.11	102.87	65.17	67.35	3.24	74.71	64.14	64.46	0.49	78.41
330°	67.82	86.90	21.95	99.79	68.75	70.02	1.81	68.83	63.32	64.59	1.97	67.58

obtained for Case-2 as described earlier, LES results are presented only for Case-2. Figure 17 illustrates the heat transfer distribution around the circumference at Sections 1–3.

There is a heat transfer enhancement at the bottom of the inner cylinder compared to the top with Case-1, indicating that the buoyant flow causes a large temperature gradient (thin boundary layer) whereas Case-2 exhibits a uniform heat transfer around the inner cylinder at Section 1. The heat transfer drop phenomenon between the bottom and top in Case-1 is one of the well-known characteristics of the pure natural convection from a

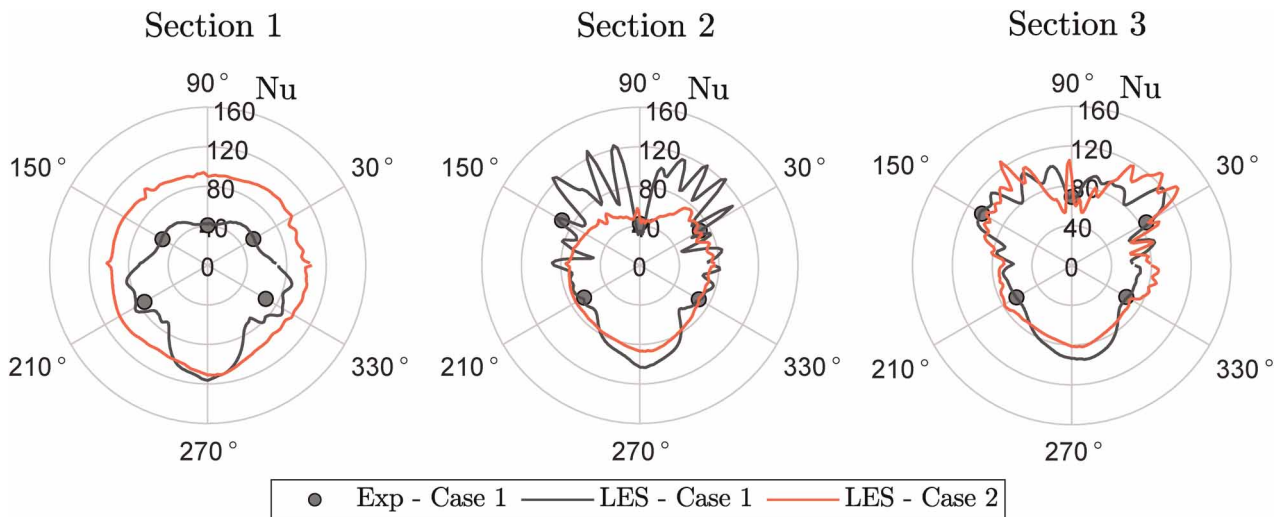


Figure 17. Heat transfer distribution around the inner cylinder.

horizontal cylinder (Kenjereš and Hanjalić, 1995), which indicates the dominance of the natural convection. There are greater heat transfer values at each sides of the cylinder than that of the top. This could be attributed to the start of formation of the side helical structures. LES results show good agreement with Case-1 experiment with a maximum error of 21.95% at $\theta = 330^\circ$.

At Section 2, the Nusselt number alternates remarkably at the upper half of the cylinder in Case-1 due to developed side structures, footprints of which are shown in Figure 16. Conversely, the bottom exhibits more uniform heat transfer rates which are slightly lower than Section 1 since the boundary layer is thicker. It is also interesting note that the minimum heat transfer has occurred at the top, indicating that the thermal plume lift-off has formed a large boundary layer. Although the highest LES error (-20.19%) has occurred at $\theta = 90^\circ$, the overall trend has been captured at Section 2. The heat transfer distribution around the inner cylinder is still uniform with Case-2 at lower rates than Section 1. This is due to the slightly thicker boundary layer.

Although there are still heat transfer minima/maxima at the upper half of the cylinder at Section 3 in Case-1, the fluctuations are not as strong as those at Section 2 since the flow is more developed at Section 3. Developing helical structures shown in Figure 16a have enhanced the heat transfer rates at both sides of the inner cylinder around 45° and 135° . The heat transfer is further reduced at the bottom as the boundary layer progressively thickens which is also valid for Case-2. Comparable heat transfer behaviour at the bottom in Case-1 and Case-2 implies that the lower half between 210° and 330° is not significantly affected by the rate at which the mixed convection occurs. On the other hand, the upper half in Case-2 now demonstrates alternating Nusselt numbers since the flow is in the region where the turbulence occurs as shown in Figure 16b. As seen in Table 8, there is a good agreement between LES and experimental results for Case-1 at Section 3.

Conclusions

This paper has presented unique experimental data for mixed (natural and forced) type of flows which occur in turbine casing cavities during shut-down regimes. Detailed measurements have been performed in axial and circumferential directions to acquire detailed information in the large majority of the test section. Two experimental campaigns with different buoyancy force dominance have been performed to investigate the mixed convection cases at different rates since the real turbine casings are exposed to various mixed type of flows during shut-down regimes. Heat flux calculations from the thermocouple measurements have been discussed and the limitations due to the viscous sub-layer thickness have been highlighted. These experimental results can be used for the validation purposes and the development of the numerical tools for complex flow interactions in mixed type of flows. Additionally, large eddy simulations have been performed and validated against the experimental data. The scale resolving simulations have provided a great insight into the flow field with distinct flow structures for each case. In Case-1 where the buoyancy was more pronounced, a developed thermal plume region was observed towards the downstream with stretched helical structures at sides. The helical structures were found to cause large

alternations in the heat transfer distribution around the inner cylinder. Case-2 where the dominance of the inertial forces was present exhibited almost circumferentially uniform boundary layer thickness. However, the varying enhanced heat transfer on the upper half of the heated inner cylinder was observed in the downstream due to the turbulent region.

These experimental and numerical results should contribute to the fundamental understanding of mixed type of flows in turbine casing cavities, which are of great importance for enabling flexible operations of the future power plants.

Nomenclature

Symbols

B	Bias error
C_p	Specific heat capacity (J/kgK)
$D_{i/o}$	Inner/Outer diameter (m)
D_h	Hydraulic diameter ($D_o - D_i$) (m)
E	Error %
f	Frequency (Hz)
k	Thermal conductivity (W/mK)
g	Gravitational acceleration (m/s^2)
h	Heat transfer coefficient (W/m^2K)
Gr	Grashof number
L_g	Gap width (m)
Nu	Nusselt number
Pr	Prandtl number
r	Radial direction
R^2	Goodness of the fit in linear regression
Re	Reynolds number
Ri	Richardson number
S	Strain rate (1/s)
\bar{T}	Time-averaged temperature (K)
T_b	Thermocouple bead temperature (K)
T_{eff}	Effective surrounding temperature (K)
T_f	True fluid temperature (K)
$\bar{\tau}_\omega$	Time-averaged wall shear stress (pascal)
U	Uncertainty %
V	Variable
Q	Second invariant of velocity ($1/s^2$)
W	Vorticity magnitude (1/s)
q''	Heat flux (W/m^2)
u	Velocity (m/s)
u_τ	Friction velocity (m/s)
ε_b	Emissivity
β	Thermal expansion coefficient (1/K)
ν	Kinematic viscosity (m^2/s)
θ	Angle ($^\circ$) or circumferential direction
σ	Stefan-Boltzmann constant ($5.6703 \times 10^{-8} (W/m^2K^4)$)

Acronyms

LES	Large eddy simulation
SGS	Sub-grid scale
HP	High pressure
RANS	Reynolds-averaged Navier-Stokes

Acknowledgments

Support from Wesley Ramm and other staff/technicians at Oxford Thermofluids Institute is much appreciated. The authors would like to acknowledge the use of the University of Oxford Advanced Research Computing (ARC) facility in carrying out the simulations. <http://dx.doi.org/10.5281/zenodo.22558>.

Funding sources

This work is sponsored by Mitsubishi Heavy Industries. The corresponding author is indebted to the Ministry of National Education, Republic of Turkey for the scholarship for graduate studies.

Competing interests

Oguzhan Murat declares that he has no conflict of interest. Budimir Rosic declares that he has no conflict of interest. Koichi Tanimoto declares that he has no conflict of interest. Ryo Egami declares that he has no conflict of interest.

References

- ANSYS (2020). *ANSYS Fluent Theory Guide 2020 R1*.
- Beckmann W. (1931). Die wärmeübertragung in zylindrischen gasschichten bei natürlicher konvektion. *Forschung auf dem Gebiet des Ingenieurwesens A*. 2 (5): 165–178.
- Brighton, J. A. (1963). The structure of fully developed turbulent flow in annuli. Ph.D. thesis, Purdue University.
- Brohez S., Delvosalle C., and Marlair G. (2004). A two-thermocouples probe for radiation corrections of measured temperatures in compartment fires. *Fire Safety Journal*. 39 (5): 399–411.
- Ciampi M., Faggiani S., Grassi W., Tuoni G., and Incropera F. (1987). Mixed convection heat transfer in horizontal, concentric annuli for transitional flow conditions. *International Journal of Heat and Mass Transfer*. 30 (5): 833–841.
- Fahy, D. D., Ireland, P. T., Lewis, L. V. and Raya, E. (2018). A novel experimental technique for investigating natural convective heat transfer in a gas turbine annulus. In Proceedings of the ASME Turbo Expo 2018: Turbomachinery Technical Conference and Exposition Volume 5B: Heat Transfer.
- Farias M. H., Braga C. V., and de Souza Mendes P. R. (2009). Heat transfer coefficients for the laminar fully developed flow of viscoplastic liquids through annuli. *International Journal of Heat and Mass Transfer*. 52 (13): 3257–3260.
- Germano M., Piomelli U., Moin P., and Cabot W. (1990). A dynamic subgrid-scale eddy viscosity model. *Physics of Fluids*. 3: 1760–1765.
- Grigull U. and Hauf W. (1966). Natural convection in horizontal cylindrical annuli, Vol. 2, 182–195.
- Hosseini R., Ramezani M., and Mazaheri M. (2009). Experimental study of turbulent forced convection in vertical eccentric annulus. *Energy Conversion and Management*. 50 (9): 2266–2274.
- Kenjereš S. and Hanjalić K. (1995). Prediction of turbulent thermal convection in concentric and eccentric horizontal annuli. *International Journal of Heat and Fluid Flow*. 16 (5): 429–439.
- Kim C. S., Hong S.-D., Seo D.-U., and Kim Y.-W. (2010). Temperature measurement with radiation correction for very high temperature gas. In 2010 14th International Heat Transfer Conference, Vol. 4, pp. 99–104.
- Kotake S. and Hattori N. (1985). Combined forced and free convection heat transfer for fully-developed laminar flow in horizontal annuli. *International Journal of Heat and Mass Transfer*. 28 (11): 2113–2120.
- Kuehn T. and Goldstein R. (1976). Correlating equations for natural convection heat transfer between horizontal circular cylinders. *International Journal of Heat and Mass Transfer*. 19 (10): 1127–1134.
- Liu C., Mueller W. K., and Landis F. (1961). Natural convection heat transfer in long horizontal cylindrical annuli. *ASME Int. Develop. Heat Transfer*. 117: 976–984.
- Moffat R. J. (1988). Describing the uncertainties in experimental results. *Experimental Thermal and Fluid Science*. 1 (1): 3–17.
- Mohammed H., Campo A., and Saidur R. (2010). Experimental study of forced and free convective heat transfer in the thermal entry region of horizontal concentric annuli. *International Communications in Heat and Mass Transfer*. 37 (7): 739–747.
- Murat O., Rosic B., Tanimoto K., and Egami R. (2021). Experimental and numerical study for improved understanding of mixed-convection type of flows in turbine casing cavities during shut-down regimes. *Journal of Engineering for Gas Turbines and Power*. 143 (12). <https://doi.org/doi: 10.1115/1.4052026>
- Schlichting H. and Gersten K. (2017). *Boundary-Layer Theory*.
- Tagawa M. and Ohta Y. (1997). Two-thermocouple probe for fluctuating temperature measurement in combustion—rational estimation of mean and fluctuating time constants. *Combustion and Flame*. 109 (4): 549–560.